Highly sensitive magnetic field sensor with normal-incidence geometry using Ni-based bilayer subwavelength periodic structure operating in visible-wavelength region

Yuusuke Takashima[1,2*], Masanobu Haraguchi[1], and Yoshiki Naoi[1]

[1]*Graduate School of Technology, Industrial and Science, Tokushima University, 2-1 Minami-josanjima, Tokushima 770-8506, Japan*

[2]*Research Fellow of Japan Society for the Promotion of Science, Japan Society for the Promotion of Science, 5-3-1 Kojimachi, Chiyoda, Tokyo 102-0083, Japan*

[*]E-mail: takashima@ee.tokushima-u.ac.jp

We successfully demonstrate a highly sensitive optical sensor for detecting magnetic fields with normal-incidence geometry that uses a Ni-based bilayer subwavelength periodic structure (SWS) operating in the visible-wavelength region. The electromagnetic field distribution within the SWS as calculated by the finite-difference time-domain method indicates that the bilayer SWS has the potential to detect minuscule magnetic fields without the need for a complex incidence system. Our bilayer Ni-SWS system with its very simple normal incidence geometry is experimentally able to detect magnetic field changes of the order of a few millitesla.

1. Introduction

Magnetic field sensing forms one of the most important techniques in engineering applications, particularly in the areas of aerospace, aviation, and controlled nuclear fusion. Highly sensitive magnetic field sensors with compact device sizes can yield advances in various integration applications, for example, integration circuit (IC) current sensing.[1)] For realizing such applications, features such as millitesla-level sensitivity, compact device size, and simple measurement systems are essential.

Hall sensors, which convert an applied magnetic field into an electrical voltage or a current, have been widely used for sensing minuscule magnetic fields. Although Hall-element-based magnetic sensors can provide a high sensitivity of a few microtesla,[2-5)] their sensitivity is strongly influenced by the measuring environment. Meanwhile, other research groups have developed extremely sensitive magnetic sensors with sensitivity of a few femtotesla with the use of superconducting quantum interference devices (SQUIDs)[6,7)] and giant magneto resistive (GMR) elements.[8)] However, setting up the measuring environment for these magnetic sensors is extremely cumbersome because of the need for cryogenic temperatures, and further, these sensors are not suitable for practical use in integrated magnetic sensing applications. Recently, optical magnetic sensors constituting magnetic-fluid-based Bragg fibers,[9,10)] photonic-crystal fibers,[11,12)] Fabry–Perot fiber interferometers,[13-15)] Mach–Zehnder interferometers,[16,17)] and taper-like fibers[18)] have been reported. Although these sensors composed of magnetic fluid and optical fiber can sense magnetic fields of the order of a few millitesla to microtesla with a short response time, they require specialized fiber-optical setups or oblique optical incidence geometry, which are impractically large for application to integration devices. For the integration application of magnetic sensors, a highly sensitive magnetic sensor with a simple geometry is highly desirable due to its compact device size and ease of setup.

In order to realize such a magnetic sensor, we focus on a magnetic field sensor using normal light incident on a subwavelength periodic structure (SWS). The period of an SWS is shorter than the incident wavelength, and the behavior of light within the SWS is different from that in free space. In an SWS, the eigenmodes resulting from its periodic refractive index distribution exist as a solution to Maxwell's equations. These modes interact with the incident light, and they are excited when the wavenumber vectors of both the incident light and eigenmodes match each other. [19,20)] This interaction can be utilized to realize extraordinary properties such as broadband high reflectivity,[21,22)] high polarization selectivity,[23-25)] high quality factor resonance,[26,27)] high numerical aperture lensing

effects,[28,29] and highly sensitive refractive index sensing[30,31] with a very simple normal-incidence geometry. The optical properties of the eigenmode strongly reflect the refractive index distribution of the SWS. The distribution of the periodic refractive index is determined by permittivity ε and permeability μ of the material constituting the SWS. Hence, the optical properties of the SWS sensitively change with variation in ε or μ of the material constituting the SWS. In this context, Karvounis et al. realized an optical switching device operating in the visible-wavelength region via controlling parameter ε of a phase-shift-material-based SWS.[32] On the other hand, non-unity μ values have been achieved in the optical frequency range with the use of inductive magnetic resonance in metal-based SWSs such as split-ring resonators.[33] However, control of permeability μ was realized only for alternating magnetic fields, and further, complex nanostructures and experimental systems are required for such approaches.

In previous study, we tried to develop magnetic field sensor using SWS.[34] In this work, we provide deep insight into SWS for magnetic sensing and successfully demonstrate a new platform for DC magnetic field sensing using a Ni-based bilayer SWS operating in the visible-wavelength region. We calculate the electromagnetic field distribution in the SWS using the three-dimensional finite-difference time-domain (3D-FDTD) method in order to estimate the magnetic field sensor performance of the designed SWS. The bilayer ferromagnetic SWS is fabricated by electron beam (EB) lithography techniques, and a minuscule magnetic field is experimentally measured using the fabricated SWS in conjunction with a very simple normal-incidence optical geometry.

2. Design concept of bilayer SWS for magnetic field sensing

In this section, we explain the operation principle of the proposed magnetic field sensor using the ferromagnetic-material-based bilayer SWS. Figure 1 shows the schematic of our proposed bilayer SWS. The bilayer SWS is positioned on a transparent thin-film grown on the substrate, and the upper and lower SWS layers are separated by a separating material. Symbols Λ, w, d, and t in Fig. 1 correspond to the grating period, ridge width, separation length between upper and lower SWS layers, and thickness of ferromagnetic material, respectively. The incident plane wave normally impinges the bilayer SWS. The eigenmodes resulting from the periodic refractive index distribution of the SWS can be excited by the use of a normal-incidence system when the wavenumber matching condition between the incident light and the eigenmodes is satisfied.[20] The excited eigenmodes interfere between

the upper and the lower SWS layers with separation length d, and the interference determines the optical response of the bilayer SWS, such as the transmission and reflection spectra.[35] The propagation properties of the excited modes such as the mode phases are strongly influenced by the periodic refractive index distribution of the SWS ridges.[20] When an external magnetic field is applied to the bilayer ferromagnetic-SWS, the refractive index of the ferromagnetic ridges of the SWS changes because the movement of electrons in the ferromagnetic material is influenced by its magnetization. Since the interference condition between the upper and lower SWS layers strongly depends on the mode phases, the reflection and transmission spectra from the bilayer ferromagnetic SWS vary with the applied external magnetic field. As a result, a minuscule magnetic field can be sensitively detected without the need for a complex measurement system, such as that with oblique incidence geometry. Further, the light transmitted through the bilayer SWS also enters the thin-film under the SWS. This light is reflected at the film–substrate interface, and thin-film interference occurs. Hence, the effect of the thin-film interference also appears in the reflection spectra from the SWS. This phenomenon is very useful for determining the change in the reflection spectra due to application of the external magnetic field.

Based on the abovementioned operation principle, we designed a bilayer SWS for a highly sensitive magnetic field sensor using the dispersion relation of the mode's wavenumber, which determines the propagation property of the eigenmode. We used the incident wavelength range of 500 nm to 550 nm (visible-wavelength range) for ease of experimentation, and Ni was employed as the ferromagnetic SWS material because a very large saturation magnetization can be obtained in nanosized Ni rods.[36] We also considered the fact that the dependence of the mode phase on the Ni refractive index change is important for sensor sensitivity because the interference between upper and lower SWS layers strongly reflects the eigenmode phase. In a previous work, the wavenumber dispersion relation of the eigenmode indicated that the period and filling factor (defined as the ratio of the grating ridge width to the period) of the SWS contributed to the propagation constant of the modes.[20] The interference between the upper and lower SWSs also depends on the separation length d. To realize high sensitivity, the propagation characteristics of the modes must be varied considerably for refractive index change in Ni to occur due to the applied external magnetic field. Referring ref. 20, the grating period, filling factor, and separation length were set to Λ = 300 nm, w = 200 nm, and d = 100 nm, respectively, in order to obtain high sensitivity in the wavelength range of 500 nm to 550 nm. The Ni thickness was set at 50 nm to prevent significant light absorption in Ni. In our study, we also used electron beam resist (ZEP 520A:

Zeon) as the separating material between the upper and lower Ni-SWSs. A GaN grown on c-sapphire substrate was used as the thin-film under the SWS because of its good chemical stability.

To estimate the magnetic sensing performance of the designed bilayer Ni-SWS, we calculated the electromagnetic field distribution using the 3D-FDTD method (Fullwave: RSoft). Figures 2(a) and (b) show the cross-sections of the FDTD calculation model for the x–z and y–z planes, respectively. In this model, the bilayer Ni-SWS was positioned on the GaN thin-film in ambient air. The perfectly matched layer (PML) boundary condition was used for the z-direction. For the x- and y-directions, a periodic boundary condition (PBC) was used because the actual length of the SWS along the x–y direction was significantly larger than the incident wavelength. The blue dashed lines in Figs. 2(a) and (b) indicate these boundaries. The calculation region was determined as the region surrounded by these boundaries. The sizes of the calculation region along the x-, y-, and z-directions were 300 nm, 2500 nm and 2 nm, respectively. The refractive indices of Ni, GaN, and sapphire were taken from the previous reports.[37-39] The space and time grids in the FDTD calculation were 2 nm and 0.46×10^{-12} s, respectively. In the model, a p-polarized plane wave, with its electric field pointed along the x-direction (Fig. 2), is considered to normally enter the bilayer Ni-SWS. The incident light propagates along the z-direction from air to the GaN region. The reflected intensity for the structure is calculated at the observation plane by means of the Poynting vector when Ni is magnetized by the external magnetic field.

Although quantum physics is necessary for strict interpretation and evaluation of the magnetization in ferromagnetic materials, we consider that the refractive index value of Ni equivalently changes with application of the magnetic field in order to roughly estimate the sensing performance of the Ni-SWS. With the assumption that free electrons mainly contribute to the optical response of Ni, the refractive index of Ni (n_{Ni}) can be expressed as the following equation from classical physics.[40]

$$n_{Ni}(\omega) = \sqrt{1 - \frac{nq^2}{m\varepsilon_0} \cdot \frac{\omega^2 + i\omega\gamma}{(\omega^2 + i\omega\gamma)^2 - \omega^2\omega_c^2}} \qquad (1)$$

Here, n, q, m, ε_0, and ω denote the electron density, electron charge, effective electron mass, permittivity in vacuum, and angular frequency of the incident wave, respectively. Further, symbol γ indicates the damping factor. Parameter ω_c in Eq. (1) is given as $\omega_c = qB/m$, where B denotes the magnetic field in Ni. From Eq. (1), we find that the refractive index of Ni

decreases with increase in the applied magnetic field.

Figure 3 shows the calculated reflectivity from the SWS as a function of the incident wavelength. The Δn_{Ni} in Fig. 3 is the amount of Ni refractive index deviation from that without the external magnetic field and is defined by

$$\Delta n_{Ni} = \ n_{Ni}(0) - n_{Ni}(B) \qquad (2)$$

Where $n_{Ni}(0)$ and $n_{Ni}(B)$ are the refractive indices of Ni without the external magnetic field and that with the field, respectively. The case without the external magnetic field corresponds to Δn_{Ni} =0. The inset in Fig. 3 depicts the magnified view of the spectra around the wavelength of 525 nm. Three reflection peaks around the wavelengths of 525 nm, 600 nm, and 675 nm can be observed in the figure. We note that when the refractive index value of Ni decreases, the peak position around 525 nm shifts to a longer wavelength while the other peaks show no significant shift. This indicates that the dispersion relation, which determines the mode phase, at 525 nm is more sensitive to the refractive index change in the grating than that at other wavelengths, as per our design. To understand the origin of the wavelength shift, we plot the y-component magnetic field (H_y) distribution at 525 nm for the cases of Δn_{Ni} = 0 and Δn_{Ni} = 0.5 in Figs. 4(a) and (b), respectively. The white squares indicate the Ni grating ridge. In the figures, the magnitude of the field amplitudes normalized by that of the incident light.

The reflection spectra from SWS are determined by average of the lateral electromagnetic field profile between the grating ridge and the air gap.[20] The incident light is partially reflected by upper SWS, and the rest is transmitted. Similarly, the transmitted light through the upper SWS is partially reflected by lower SWS and travels back. If the field amplitude of the reflected light by upper and lower SWSs are in-phase at the interface between air and upper SWS, a strong reflection appears. Thus, such interference, which determines the reflection spectra of the bilayer SWS, strongly depends on the field amplitudes in the ridge and air gap. In Fig. 4(a), the field amplitudes in the ridge and air gap region are in phase at the interface between air and the upper SWS, thereby leading to constructive interference. This interference gives rise to the reflection peak at 525 nm. On the other hand, the field amplitude at the grating and air gap changes with decrease in n_{Ni} as shown in Fig. 4(b), which corresponds to a change in the interference conditions, thereby leading to change in the reflection intensity. These calculation results indicate that our proposed SWS can detect an external magnetic field without requiring complex incidence geometry such as that of an

oblique incidence system.

3. Experimental results and discussion

We fabricated our proposed bilayer Ni-SWS by using an EB lithography technique as follows. A GaN thin-film was grown on a c-plane sapphire substrate using the metalorganic chemical vapor deposition method. A 100-nm-thick EB resist was spin-coated on the GaN, and the EB resist (ZEP520A: Zeon) was baked at 120 °C for 30 min. The SWS pattern was drawn using an EB lithography system (ELS7500: Elionix). A 50-nm-thick Ni-film was evaporated onto the patterned resist at a chamber pressure of about 2×10^{-5} Torr. The top-view scanning electron microscope (SEM) image of the fabricated bilayer Ni-SWS is shown in Fig. 5 (a). The fabricated bilayer Ni-SWS shown in the figure has structural parameters of Λ = 300 nm, w = 200 nm, d = 100 nm, and t = 50 nm. Figure 5 (b) also showed surface photograph of whole sample, and the bilayer SWS area is 300μm × 100 μm.

We measured the optical characteristics of the fabricated bilayer Ni-SWS to evaluate its magnetic sensing performance at room temperature. Figure 6 shows the measurement system utilized to measure the optical properties of the SWS. The sample was placed on the center of the solenoid coil. The DC magnetic field generated by the current was applied to the sample as shown in Fig. 6. The direction of the magnetic field was perpendicular to the sample surface (Fig. 6). The value of the applied magnetic field was measured by Gauss meter (Lake Shore 410 gauss meter). A halogen lamp was used as light source, and the light from the lamp was subsequently collimated by a collimator lens. The collimated light was p-polarized, with the electric field being parallel to the grating stripes, as shown in Fig. 2. The incident light was focused onto the Ni-SWS area by means of an objective lens (×20, NA = 0.46), and the normal reflection spectra were measured with a spectrometer when an applied DC magnetic field was increased. The irradiated area was about 100 μm × 100 μm.

The reflection spectra from the fabricated sample at normal-incidence geometry are shown in Fig. 7(a) as a function of the incident wavelength. Here, the reflection spectra from the Ni-SWS are normalized by that from a 50-nm-thick Ni-film on the GaN thin-film/sapphire substrate. In Fig. 7(a), we can observe several peaks and dips in the reflection spectra, which are formed by thin-film interference. For the case without the SWS, there is no significant shift in the reflection peak when an external magnetic field of 90 mT is applied. In contrast, as shown in Fig. 7(a), the peak position in the spectra from the bilayer Ni-SWS exhibits a significant shift towards longer wavelengths when the external magnetic field intensity increases. This experimental tendency of the measured results shows good agreement with

the predicted tendency. While the reflection peak was theoretically expected at the wavelength of 525 nm as shown in Fig. 3, the positions of the experimental reflection peaks were differ from this wavelength. This can be attributed to the difference in the refractive index values of GaN between FDTD calculation and experiment. The reflection spectra from our sample depend on not only interference in bilayer SWS but also thin-film interference in GaN film under the SWS. The value of GaN refractive index is influenced on its growth conditions[38,41], and the effective optical thickness of GaN for the incident light was varied with the change of its refractive index. As a result, the peak position of reflection spectra from the sample differ from that in the calculation. In fact, the calculated electromagnetic field distribution shows that reflection peak was founded at the wavelength of 540 nm assuming a GaN refractive index smaller by 0.1 to the value used in the FDTD calculation.

We also depict the reflection peak position around 540 nm as a function of the external magnetic field intensity in Fig. 7(b). The dashed line shows the linear fit by least squares method. We note that the peak wavelength almost linearly increases with increase in the external magnetic field intensity. When a magnetic field of 89.2 mT is applied, the peak shift value is about 1.5 nm. This result corresponds to a magnetic field sensitivity of 16.8 pm/mT, which is comparable with those of a conventional Hall element, fiber Bragg grating magnetic field sensor[10], and Fabry–Perot fiber interferometer[14]. The origin of such high sensitivity can be explained as follows. The interference conditions between the upper and lower SWS layers are determined by the phase of the excited mode within both SWSs. The permittivity of the Ni-SWS changes upon application of the external magnetic field due the magnetization of Ni. The phase variations in not only the single mode but also all excited modes between the upper and lower Ni-SWSs contribute to the interference conditions. Thus, the interference conditions significantly deviate from those in the absence of the magnetic field. As a result, high sensitivity is realized for external magnetic field sensing.

These results suggest that the sensing of minuscule magnetic fields can be successfully realized even with a simple normal-incidence experimental setup at room temperature. Thus, our proposed bilayer SWS is of great use for integration applications and as a practical magnetic field sensor.

4. Conclusions

We proposed and successfully demonstrated a high-sensitivity DC magnetic field sensor using a bilayer Ni-SWS with very simple normal-incidence geometry. The field values as calculated by the FDTD method indicated that the proposed SWS can detect magnetic fields with a normal-incidence measurement system. Our bilayer Ni-SWS was fabricated on a GaN film by means of EB lithography, and the reflection spectra from the fabricated bilayer Ni-SWS exhibited significant variation with application of an external magnetic field. The peak wavelength shift in the normal reflection spectra reached about 1.5 nm when a magnetic field of 89.2 mT was applied. This result demonstrates that our sensor can be practically used in magnetic sensing applications owing to its high sensitivity and simple experimental setup.

Acknowledgments

The work was partially supported by JSPS KAKENHI, Grant Number JP16J11232.

References

1) C. Reig, M. D. C. Beltran, and D. R. Munoz, Sensors **9**, 7919 (2009).
2) P. A. Besse, G. Boero, M. Demierre, V. Pott, and R. Popovic, Appl. Phys. Lett. **80**, 4199 (2002).
3) L. Ejsing, M. F. Hansen, A. K. Menon, H. A. Ferreira, D. L. Graham, and P. P. Freitas, Appl. Phys. Lett. **84**, 4729 (2004).
4) H. Heidari, E. Bonizzoni, U. Gatti, and F. Maloberti, IEEE Trans. Circuit Syst. **62**, 1270 (2015).
5) C. Sander, C. Leube, and O. Paul, Sens. Actuators A **248**, 281 (2016).
6) J. Gallop, Supercond. Sci. Technol. **16**, 1575 (2003).
7) H. J. Barthelmess, M. Halverscheid, B. Schiefenhovel, E. Heim, M. Schilling, and R. Zimmermann, IEEE Trans. Appl. Superconduct. **11**, 657 (2001).
8) M. Pannetier, C. Fermon, G. L. Goff, J. Simola, and E. Kerr, Science **304**, 1648 (2004).
9) J. Dai, M. Yang, X. Li, H. Liu, and X. Tong, Opt. Fiber Technol. **17**, 210 (2011).
10) D. Yang, L. Du, Z. Xu, Y. Jiang, J. Xu, M. Wang, Y. Bai, and H. Wang, Appl. Phys. Lett. **104**, 061903 (2014).
11) H. V. Thakur, S. M. Nalawade, S. Gupta, R. Kitture, and S. N. Kale, Appl. Phys. Lett. **99**, 161101 (2011).
12) P. Zu, C. C. Chan, T. Gong, Y. Jin, W. C. Wong, and X. Dong, Appl. Phys. Lett. **101**, 241118 (2012).
13) K. D. Oh, A. Wang, and R. O. Claus, Opt. Lett. **29**, 2115 (2004).
14) S. Dong, S. Pu, and J. Huang, Appl. Phys. Lett. **103**, 111907 (2013).
15) B. Cheng, L. Yuan, W. Zhu, Y. Song, and H. Xiao, Sens. Actuators A **257**, 194 (2017).
16) Z. Li, C. Liao, J. Song, Y. Wang, F. Zhu, Y. Wang, and X. Dong, Photon. Res. **4**, 197 (2016).
17) H. Liu, H. Zhang, B. Liu, B. Song, J. Wu, and L. Lin, Appl. Phys. Lett. **109**, 042402 (2016).
18) S. Dong, S. Pu, and H. Wang, Opt. Express **22**, 19108 (2014).
19) C. J. C. Hasnain, Semicond. Sci. Technol. **26**, 014043 (2011).
20) C. J. C. Hasnain and W. Yang, Adv. Opt. Photonics **4**, 379 (2012).
21) C. F. R. Mateus, M. C. Y. Huang, Y. Deng, A. R. Neureuther, and C. J. C. Hasnain, IEEE Photon. Technol. Lett. **16**, 518 (2004).
22) Y. Zhou, M. C. Y. Huang, and C. J. C. Hasnain, IEEE Photon. Technol. Lett. **20**, 434 (2008).

23) L. Zhuang, S. Schablitsky, R. C. Shi, and S. Y. Chou, J. Vac. Sci. Technol. B **14**, 4055 (1996).
24) Y. Takashima, M. Tanabe, M. Haraguchi, and Y. Naoi, Opt. Commun. **369**, 38 (2016).
25) Y. Takashima, M. Tanabe, M. Haraguchi, and Y. Naoi, Appl. Opt. **56**, 8224 (2017).
26) Y. Zhou, M. Moewe, J. Kern, M. C. Y. Huang, and C. J. C. Hasnain, Opt. Express **16**, 17282 (2008).
27) Y. Zhou, M. C. Y. Huang, C. Chase, V. Karagodsky, M. Moewe, and C. J. C. Hasnain, IEEE J. Sel. Top. Quantum Electron. **15**, 1485 (2009).
28) M. Khorasaninejad, F. Aieta, P. Kanhaiya, M. A. Kats, P. Genevet, D. Rousso, and F. Capasso, Nano Lett. **15**, 5358 (2015).
29) S. He, Z. Wang, Q. Liu, and W. Wang, Opt. Express **23**, 29360 (2015).
30) T. Sun, G. Marriott, and C. J. C. Hasnain, Sci. Rep. **6**, 27482 (2016).
31) Y. Takashima, M. Haraguchi, and Y. Naoi, Sens. Actuators B **255**, 1711 (2018).
32) A. Karvounis, B. Gholipour, K. F. Macdonald, and N. I. Zheludev, Appl. Phys. Lett. **109**, 051103 (2016).
33) T. Amemiya, T. Shido, D. Takahashi, S. Myoga, N. Nishiyama, and S. Arai, Opt. Lett. **36**, 2327 (2011).
34) Y. Takashima, M. Haraguchi, and Y. Naoi: MOC Tech. Dig., 2017, p. 256.
35) Y. Ekinci, H. H. Solak, C. David, and H. Sigg, Opt. Express. **14**, 2323 (2006).
36) R. Ferre, K. Ounadjela, J. M. George, L. Piraux, and S. Dubois, Phys. Rev. B **56**, 14066 (1997).
37) P. B. Johnson and R. W. Christy, Phys. Rev. B **9**, 5056 (1974).
38) A. S. Barker Jr. and M. Ilegems, Phys. Rev. B **7**, 743 (1973).
39) I. H. Malitson and M. J. Dodge, J. Opt. Soc. Am. **62**, 1405 (1972).
40) G. Dresselhaus, A. F. Kip, and C. Kittel, Phys. Rev. **100**, 618 (1955).
41) M. E. Lin, B. N. Sverdlov, S. Strite, H. Morkoc, and A. E. Drakin, Electron. Lett. **29**, 1759 (1993).

Figure Captions

Fig. 1. (Color online) Schematic of ferromagnetic-material-based bilayer subwavelength periodic structure (SWS).

Fig. 2. (Color Online) Three-dimensional finite-difference time-domain (3D-FDTD) numerical calculation model: (a) x–z plane and (b) y–z plane cross-sections.

Fig. 3 (Color Online) Finite-difference time-domain (FDTD)-calculated reflectivity of bilayer Ni subwavelength periodic structure (Ni-SWS) as function of incident wavelength.

Fig. 4 (Color Online) Magnetic field distribution in subwavelength periodic structure (SWS) at wavelength of 525 nm: (a) for $\Delta n_{Ni} = 0$ and (b) for $\Delta n_{Ni} = 0.5$. The white squares indicate the Ni grating ridge. The field amplitude is normalized by that of the light source.

Fig. 5 (Color Online) (a) Top-view scanning electron microscope image of fabricated bilayer Ni subwavelength periodic structure (Ni-SWS) and (b) surface photograph of whole sample.

Fig. 6 (Color Online) Experimental measurement system to obtain reflection spectra from fabricated Ni subwavelength periodic structure (Ni-SWS).

Fig. 7 (Color Online) (a) Reflection spectra from fabricated bilayer Ni subwavelength periodic structure (Ni-SWS) and (b) peak position around wavelength of 540 nm as function of external magnetic field intensity.

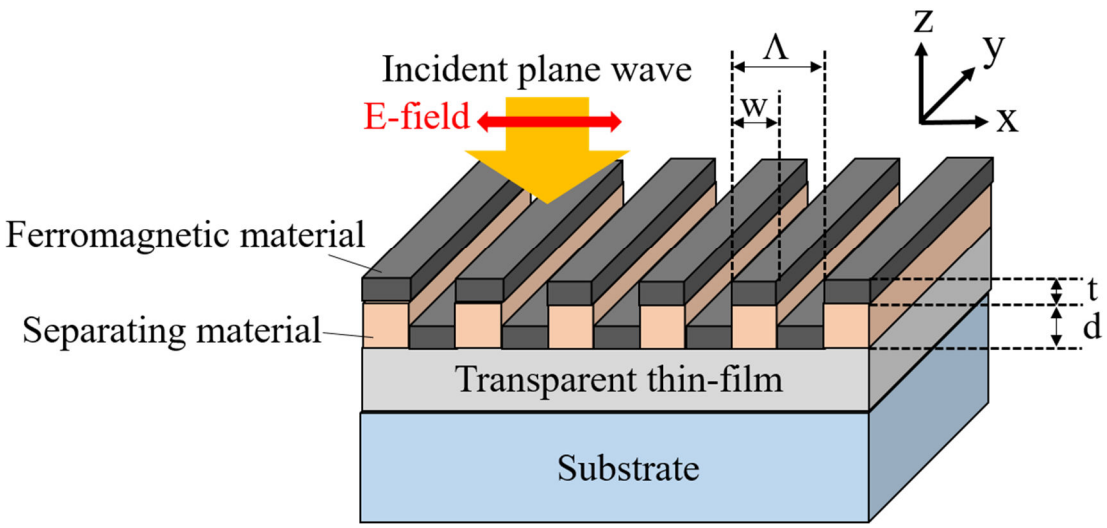

Fig. 1. (Color Online)

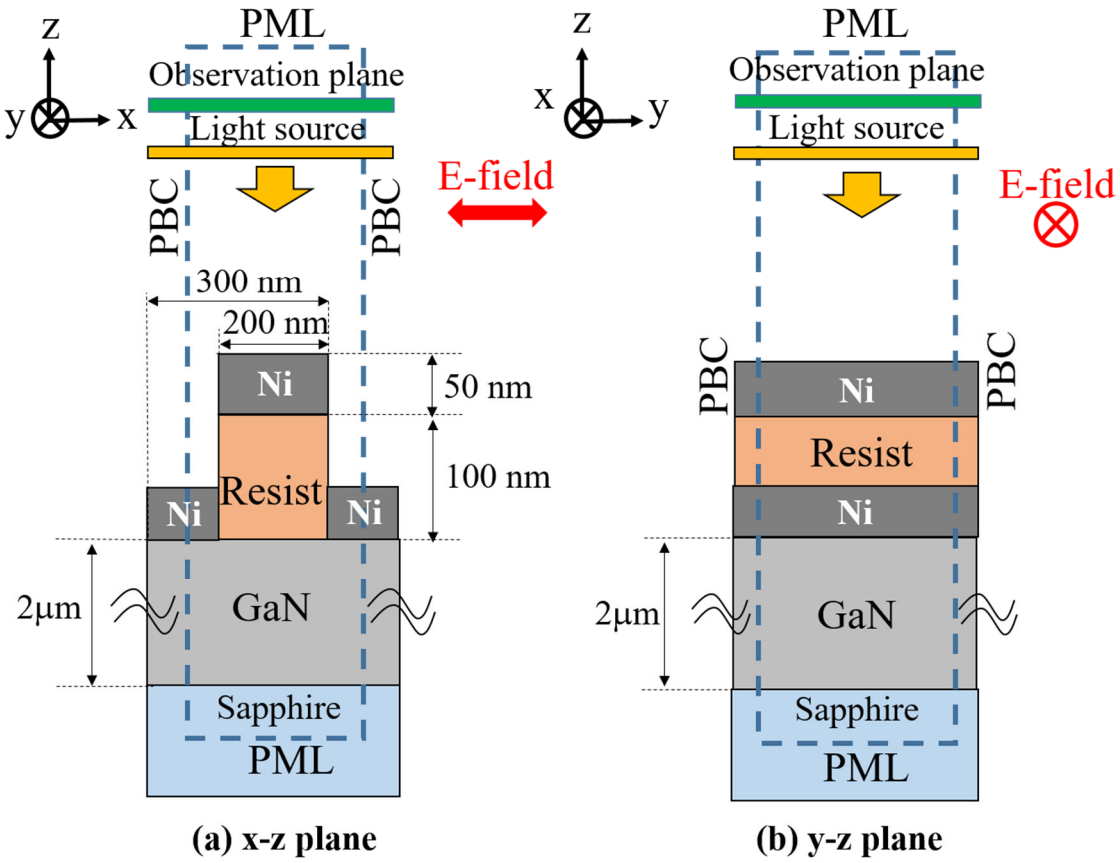

Fig. 2. (Color Online)

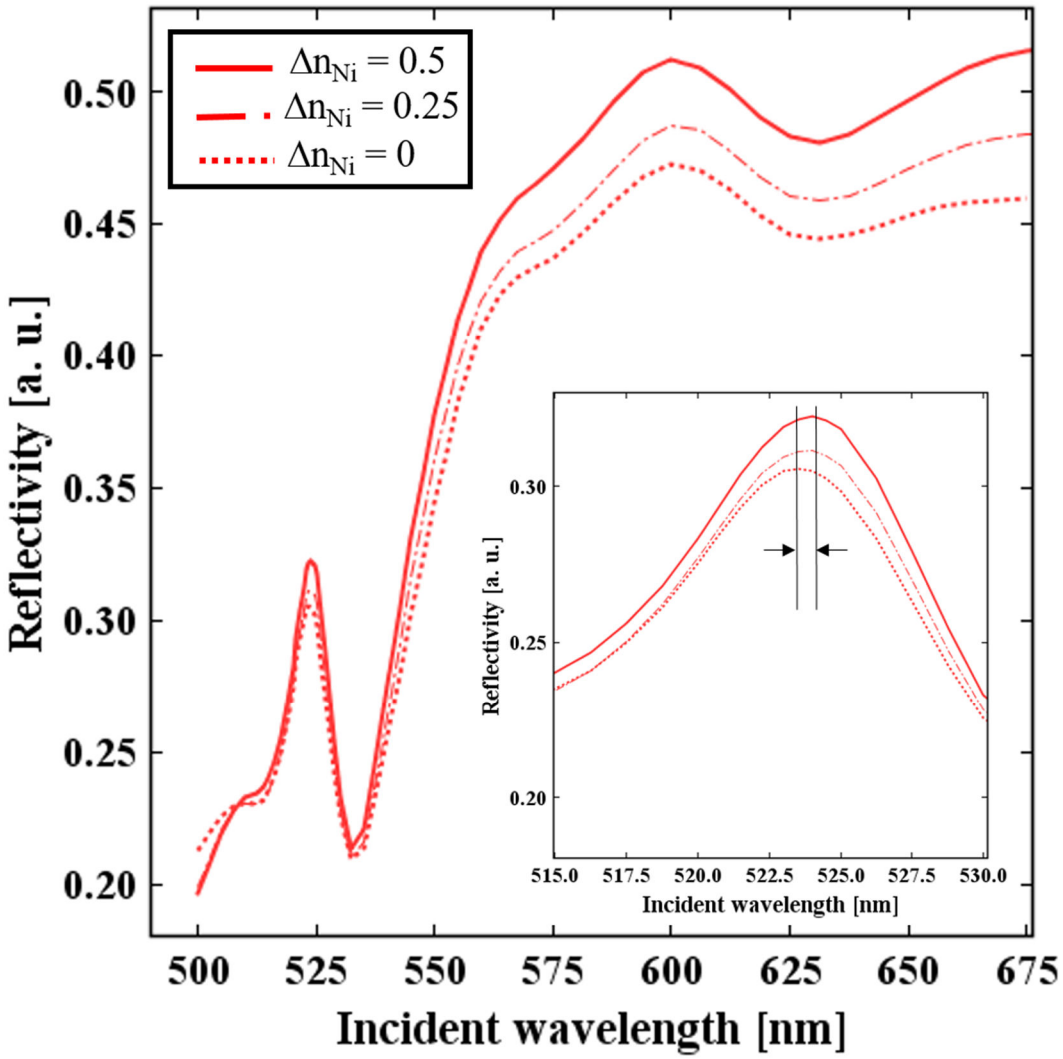

Fig. 3. (Color Online)

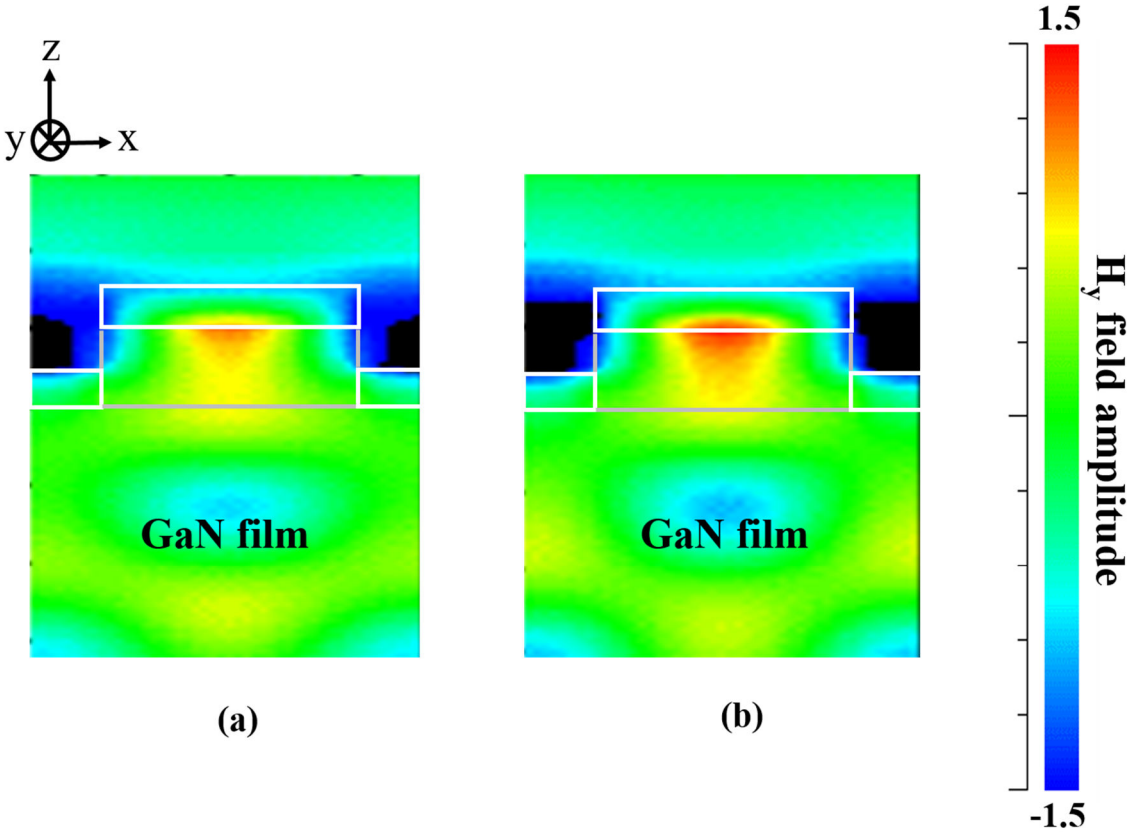

Fig. 4. (Color Online)

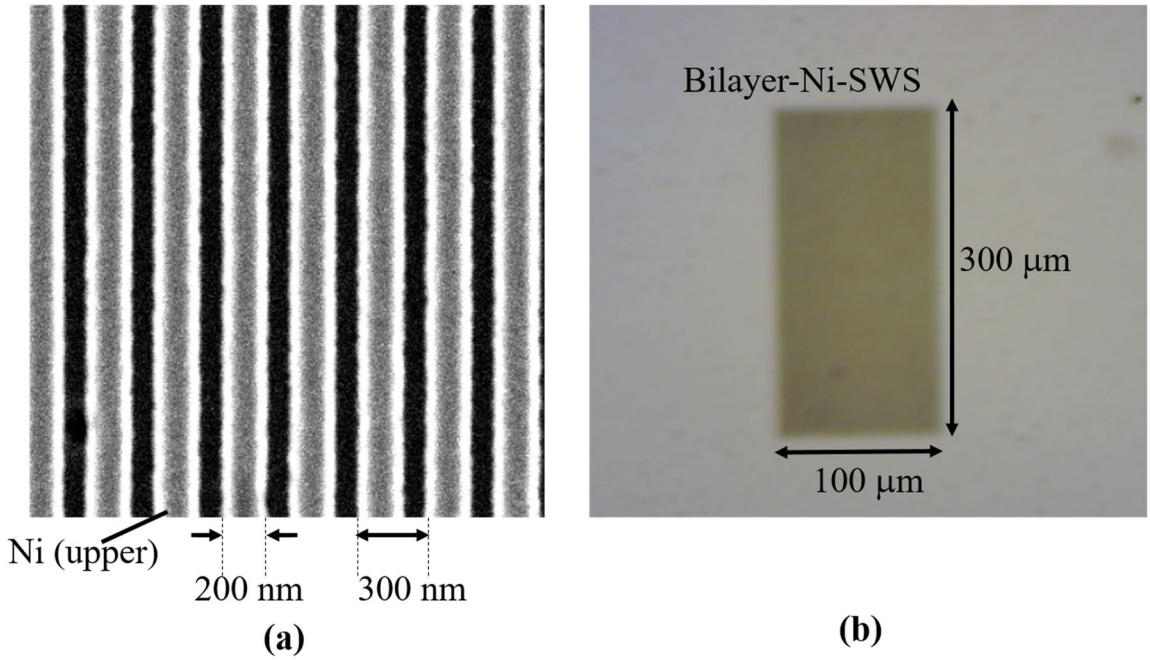

Fig. 5. (Color Online)

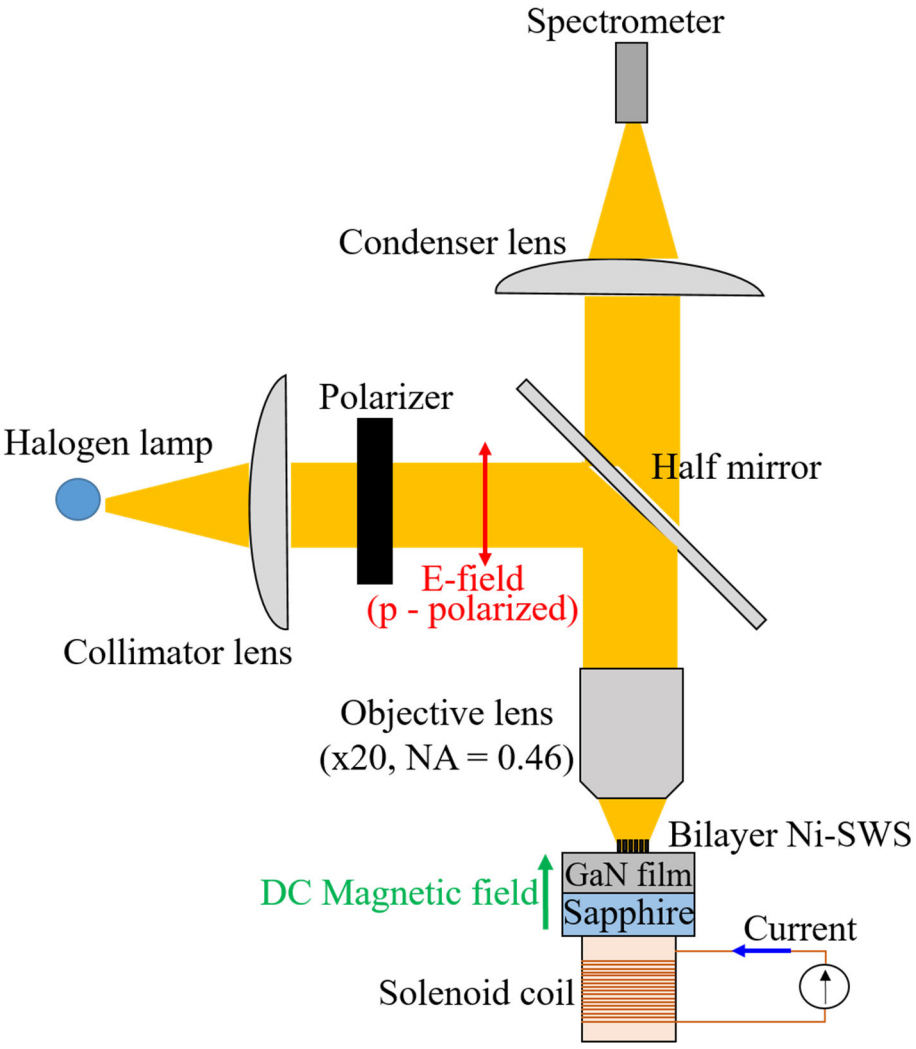

Fig. 6. (Color Online)

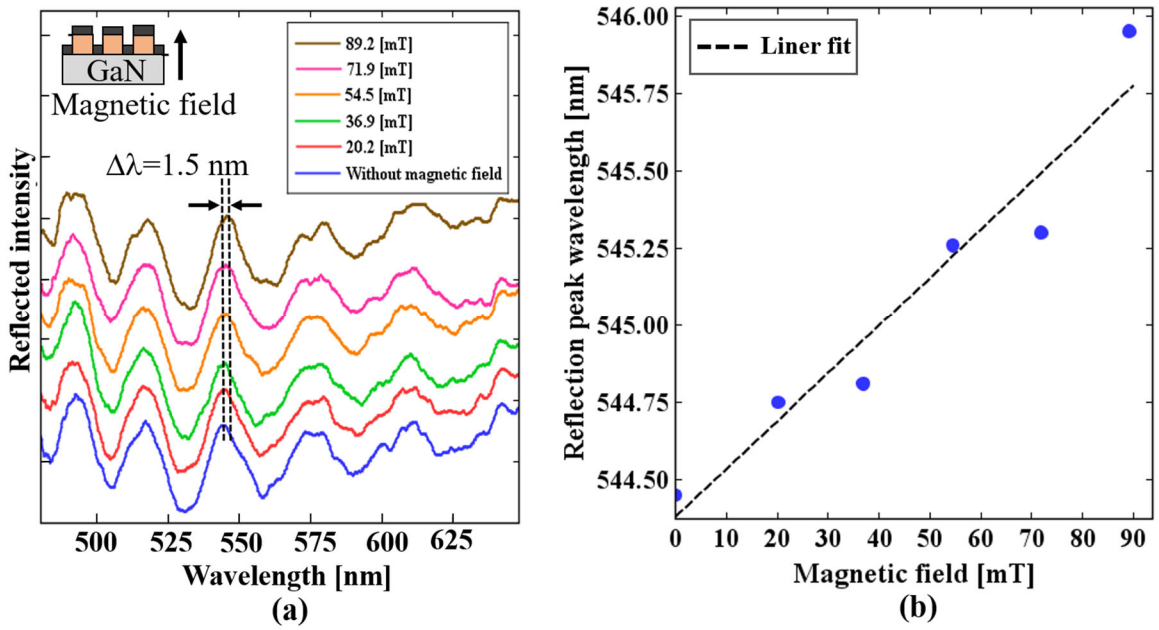

Fig. 7. (Color Online)